

Thermodynamics of Blue Phases In Electric Fields

O. Henrich¹, D. Marenduzzo¹, K. Stratford², M. E. Cates¹

¹ SUPA, School of Physics and Astronomy, The University of Edinburgh,
JCMB, King's Buildings, Mayfield Road, Edinburgh EH9 3JZ, UK

EPCC, The University of Edinburgh, JCMB, King's Buildings, Mayfield Road, Edinburgh EH9 3JZ, UK

(Dated: November 10, 2018)

We present extensive numerical studies to determine the phase diagrams of cubic and hexagonal blue phases in an electric field. We confirm the earlier prediction that hexagonal phases, both 2 and 3 dimensional, are stabilized by a field, but we significantly refine the phase boundaries, which were previously estimated by means of a semi-analytical approximation. In particular, our simulations show that the blue phase I – blue phase II transition at fixed chirality is largely unaffected by electric field, as observed experimentally.

PACS numbers: 61.30.Mp, 64.60.qe

I. INTRODUCTION

The blue phases (BPs) of chiral molecules provide spectacular examples of soft solids, formed via a spontaneously occurring network of disclination lines within a cholesteric background [1]. All BPs arise close to the transition between the cholesteric and the isotropic phase; in at least two cases (BPI and BPII) the disclination network forms an ordered (cubic) lattice. (A third, BPIII, is thought to be amorphous [1].) When an electric field is applied, several new blue phase disclination lattices have either been observed or theoretically predicted. Two of these have hexagonal symmetries, and have been named H_{2D} and H_{3D} respectively: these have first been predicted theoretically [2, 3] and subsequently seen experimentally [4]. A further BP appearing in a field, BPX, has tetragonal symmetry: it was found experimentally in the 1980s [5] and its structure recently possibly revealed by simulations [6]. For a review of experimental results on blue phases, especially in electric fields, the interested reader should consult Refs. [7, 8].

In the last few years, BPs have emerged as very promising device materials with fast (sub- μ s) and tunable color response. This increase in technological potential comes from recent remarkable experiments [9–11], which managed to stabilize BPs over a temperature range of 50 K, compared to ranges of about 1 K previously [1]. However, for their potential to be fully realized, our understanding of BPs needs to become as quantitative as the one we have for conventional nematic liquid crystals.

In particular, our theoretical knowledge of the phase diagrams of BP-forming liquid crystals in the presence of an applied field is currently quite dated. It relies on the seminal papers by Hornreich *et al.* [2, 3], which are however based on an approximation (to allow semi-analytical progress): the tensorial liquid crystalline order parameter is represented by a Fourier series, comprising harmonics of relatively high order but only corresponding to the $m = 2$ helicity mode, which eliminates the dependence on one of the elastic constants (see Refs. [12, 13] for details). These papers have provided a very useful first theory of blue phases, but it has become clear recently

that their quantitative predictive power is somewhat limited [6, 12, 14, 15]. For instance, within these approximations, the phase diagram at zero electric field predicts that BPII and BPI appear in the wrong order upon varying the molecular chirality [12] (cf. experimental phase diagrams shown in, e.g., Ref. [8]). At the same time, these theories were also unable to account for anomalous electrostriction of BPI [6, 16, 17]. Recent simulations have shown that these shortfalls are a drawback of the approximations employed, and not of the underlying Landau – de Gennes mean field free energy [18]. The latter is the starting point for describing the thermodynamics of BPs, and when handled directly gives good semi-quantitative agreement with the experiments. The simulations of Refs. [15, 19] use a lattice Boltzmann (LB) method which can address the full dynamics of the system including fluid flow. Recent work favors instead a hybrid method [20, 21] in which an LB code for fluid degrees of freedom is coupled to a conventional finite difference code for the order parameter (this method was recently used in binary fluids as well [22]). In the current work, we address only thermodynamic steady states, in which case it is convenient to switch off the fluid motion and use only diffusive relaxation to find local minima of the free energy. (We can then compare these minima to construct the phase diagram.) As well as being directly comparable with experiments, the resulting phase diagrams form a secure foundation for future hydrodynamic simulations on the same systems using the hybrid LB approach [21].

Our program in this paper is therefore to update the phase diagrams for blue phases in an electric field by computer simulation of the governing equations derived from the Landau – de Gennes free energy functional (detailed below). We find that the existing semi-analytical approximations [2, 13, 23] are able to capture rather well the qualitative physics of the problem. In particular, we confirm that an intermediate electric field stabilizes the two previously proposed hexagonal phases, H_{2D} and H_{3D} . However, our simulations show that the blue phases, whether cubic or hexagonal, extend to regions of significantly lower chirality than predicted by the

semi-analytical approximation; this in agreement with the trend which was observed in phase diagrams of BPs without any electric field [14, 15]. Furthermore, we also resolve which of the cubic blue phases, BPI or BPII, is stable at any given point in the phase diagram. Hence we find that the Landau – de Gennes free energy leads to a near-horizontal phase boundary in the field-temperature plane, in agreement with experimental observations [24].

It is important to note that, while in this work we focus on a continuum description of blue phase via a Landau – de Gennes free energy, there also exist simulation studies of individually resolved molecules, described as spherocylinders interacting with a coarse grained potential [25], which managed to stabilize blue phases. This approach is extremely interesting, however the length and time scales accessible within it are significantly smaller than the ones we can cover with our approach, and it would be unfeasible to compute a phase diagram with this method.

This paper is organized as follows. In Section II we discuss the Landau – de Gennes theory which leads to the continuum equation of motion which we numerically solve. In Section III we present the numerical results, i.e. the phase diagrams in the chirality-temperature and temperature-field, planes, and we quantitatively compare them with the ones predicted via semi-analytical approximations. Finally, Section IV contains our discussion and conclusions.

II. LANDAU – DE GENNES THEORY

A. Equations of motion and free energy

The nematodynamic description of liquid crystals, often named after its inventors as the Erickson-Leslie-Parodi approach, uses a fixed-magnitude (headless) unit vector field as order parameter. This “director field” represents the average orientation of the liquid crystal molecules. However, this approach proves to be inappropriate for BPs, as it cannot account for disclination lines: on these topological defects, the strength of nematic ordering goes to zero and no average local orientation can be defined. A suitable description of BPs is therefore only possible within the framework of the Landau – de Gennes theory. This employs an order parameter \mathbf{Q} , which is a traceless and symmetric second rank tensor; this can describe simultaneously the direction and magnitude of local nematic ordering. The Q-tensor approach also allows for this ordering to become biaxial; in general the order parameter can be written as:

$$\mathbf{Q} = q_l(\vec{l} \otimes \vec{l}) + q_m(\vec{m} \otimes \vec{m}) - \frac{1}{3}(q_l + q_m)\mathbf{I}, \quad (1)$$

where \otimes denotes the tensorial product. The vector fields \vec{l} and \vec{m} are two independent director fields perpendicular to each other. The quantities q_l and q_m are called the scalar order parameters and \mathbf{I} is the unit tensor. This representation confirms \mathbf{Q} to be a traceless symmetric

second rank tensor which has five independent components. In many systems the smaller of the two scalar order parameters is everywhere very small (if not strictly zero). A director field \vec{n} and a scalar order parameter q can then be reintroduced within the *uniaxial approximation*:

$$\mathbf{Q} \approx q(\vec{n} \otimes \vec{n}) - \frac{q}{3}\mathbf{I}. \quad (2)$$

This now has three independent components to describe both the strength and the director of the uniaxial ordering. However, we have no need for the uniaxial approximation in the numerical approach used in this paper.

The phenomenological Landau – de Gennes free energy functional in an external electric field \mathbf{E} is given as:

$$\begin{aligned} \mathcal{F}[\mathbf{Q}] = & \int d^3r \left\{ \frac{A_0}{2} \left(1 - \frac{\gamma}{3}\right) Q_{\alpha\beta}^2 - \frac{A_0\gamma}{3} Q_{\alpha\beta} Q_{\beta\gamma} Q_{\gamma\alpha} \right. \\ & + \frac{A_0\gamma}{4} (Q_{\alpha\beta}^2)^2 - \frac{\epsilon_a}{12\pi} E_\alpha Q_{\alpha\beta} E_\beta \\ & \left. + \frac{K}{2} [(\epsilon_{\alpha\gamma\delta} \partial_\gamma Q_{\delta\beta} + 2q_0 Q_{\alpha\beta})^2 + (\partial_\alpha Q_{\alpha\beta})^2] \right\} \quad (3) \end{aligned}$$

The thermodynamic equilibrium state is the global minimum of \mathcal{F} for any given parameters; metastable phases are local minima of \mathcal{F} . The complete free energy is made up of three different contributions. The first one (comprising all terms containing A_0) is the bulk free energy, which contains terms of the Q-tensor up to fourth order. The scale factor A_0 is called the bulk free energy constant, while the parameter γ plays the role of an effective reciprocal temperature. For a nematogen without chirality ($q_0 = 0$), for $\gamma < 2.7$ the isotropic state gives the global minimum of the free energy, whereas for $\gamma \geq 2.7$ the system has nematic order in equilibrium. The relative local distortion enters the free energy functional on the level of first order gradient terms; throughout this paper we consider only the “one elastic constant” approximation [18], which is a common approach when investigating generic liquid crystallizing behavior. K is the resulting single elastic constant; without this approximation, Eq. 3 becomes considerably more complicated. We have chosen a specific representation of the gradient free energy [1], which incorporates a gradient-independent part of the bulk free energy to ensure that it is always positive. The parameter $q_0 = \frac{2\pi}{p_0}$ determines the intrinsic preferred pitch length p_0 of the underlying cholesteric (*i.e.*, chiral nematic) liquid crystal. Thirdly, the coupling to an external electric field E_α is provided by the remaining term in Eq. 3, with $\epsilon_a > 0$ being the dielectric anisotropy. This term is linear in the Q-tensor and quadratic in the electric field (the latter is dictated by symmetry for non-ferroelectric liquid crystals, as considered here).

For the purposes of finding local minima of \mathcal{F} it is sufficient to ignore fluid flow and momentum conservation, instead taking the tensor order parameter \mathbf{Q} to obey the following (purely relaxational) equation of motion:

$$\frac{\partial \mathbf{Q}}{\partial t} = \Gamma \mathbf{H}. \quad (4)$$

The molecular field \mathbf{H} is defined as the functional derivative of the Landau – de Gennes free energy functional Eq. 3 with respect to the order parameter, and therefore it vanishes in equilibrium. It is specifically given by:

$$\mathbf{H} = -\frac{\delta\mathcal{F}}{\delta\mathbf{Q}} + \frac{\Gamma}{3} \text{Tr} \left(\frac{\delta\mathcal{F}}{\delta\mathbf{Q}} \right) \quad (5)$$

The parameter Γ is a rotational diffusion constant. (Note that in practice Eq. 4 is supplemented by an additional dynamical update rule for a so-called ‘redshift’ factor, described below.)

It is convenient to render the free energy functional Eq. 3 dimensionless. This gives rise to the following minimal set of parameters on which phase behavior can depend:

$$\tau = \frac{27(1 - \gamma/3)}{\gamma} \quad (6)$$

$$\kappa = \sqrt{\frac{108 K q_0^2}{A_0 \gamma}} \quad (7)$$

$$e^2 = \frac{27\epsilon_a}{32\pi A_0 \gamma} E_\alpha E_\alpha. \quad (8)$$

Note that the cholesteric pitch parameter q_0 is used in the non-dimensionalization of lengths; clearly this works only for nonzero q_0 which we from now on assume. (There are no BPs for achiral molecules with $q_0 = 0$.) The quadratic term of the dimensionless bulk free energy becomes then proportional to the reduced temperature τ , whereas the magnitude of the gradient free energy term is proportional to κ , the chirality. Note that the chirality κ expresses a ratio between the gradient free energy and the bulk free energy terms and is a measure of how much twist the system wants to have. The parameter e is an effective field strength.

The free energy functional Eq. 3 yields a highly complicated free energy landscape. Although the equilibrium state for each τ, κ, e is uniquely defined by the functional, it is not generally possible to determine these states by any analytical minimization procedure. An exception is the limit of infinite chirality, where the bulk as well as the external field free energy terms become negligible compared to the gradient free energy and an analytical solution can be found. While this limit of infinite chirality is hardly relevant for a real-world understanding or experiments, the topological character of the equilibrium defect structure in this limit is often unaltered upon reducing chirality – so long as the unit of length (related to q_0) is rescaled appropriately. Therefore, these analytical solutions offer a useful starting point for numerical solutions of the relaxational dynamics: one can initialize the runs at finite chirality with the solution that is already known for the infinite chirality limit. The chosen dynamics will relax this structure towards a local free energy minimum; we then compare the minimized free energy with those found from competing starting structures to find the best possible local minimum among the ones corresponding to the topologies which we have considered.

B. Initial conditions

In this work we consider four such structures, alongside the isotropic phase, the (para-)nematic phase, and the standard uniaxial configuration for the cholesteric state: BPI, BPII, H_{2D} and H_{3D} (in this last case we consider two possible starting conditions, labeled H_{3D}^a and H_{3D}^b). In each case the relevant infinite-chirality expression was taken as initial conditions. For BPI we used:

$$\begin{aligned} Q_{xx} &\simeq -2 \cos(q'_0 y) \sin(q'_0 z) + \\ &\quad \sin(q'_0 x) \cos(q'_0 z) + \cos(q'_0 x) \sin(q'_0 y) \\ Q_{xy} &\simeq \sqrt{2} \cos(q'_0 y) \cos(q'_0 z) + \\ &\quad \sqrt{2} \sin(q'_0 x) \sin(q'_0 z) - \sin(q'_0 x) \cos(q'_0 y) \\ Q_{xz} &\simeq \sqrt{2} \cos(q'_0 x) \cos(q'_0 y) + \\ &\quad \sqrt{2} \sin(q'_0 z) \sin(q'_0 y) - \cos(q'_0 x) \sin(q'_0 z) \\ Q_{yy} &\simeq -2 \sin(q'_0 x) \cos(q'_0 z) + \\ &\quad \sin(q'_0 y) \cos(q'_0 x) + \cos(q'_0 y) \sin(q'_0 z) \\ Q_{yz} &\simeq \sqrt{2} \cos(q'_0 z) \cos(q'_0 x) + \\ &\quad \sqrt{2} \sin(q'_0 y) \sin(q'_0 x) - \sin(q'_0 y) \cos(q'_0 z), \end{aligned} \quad (9)$$

where $q'_0 = \sqrt{2}q_0$. For BPII we used:

$$\begin{aligned} Q_{xx} &\simeq \cos(2q_0 z) - \cos(2q_0 y); \quad Q_{xy} \simeq \sin(2q_0 z) \\ Q_{xz} &\simeq \sin(2q_0 y); \quad Q_{yy} \simeq \cos(2q_0 x) - \cos(2q_0 z) \\ Q_{yz} &\simeq \sin(2q_0 x). \end{aligned} \quad (10)$$

For the hexagonal two-dimensional BP, abbreviated as H_{2D} , we used:

$$\begin{aligned} Q_{xx} &\simeq -\frac{3}{2} \cos(q_0 x) \cos(\sqrt{3}q_0 y) \\ Q_{xy} &\simeq -\frac{\sqrt{3}}{2} \sin(q_0 x) \sin(\sqrt{3}q_0 y) \\ Q_{xz} &\simeq \sqrt{3} \cos(q_0 x) \sin(\sqrt{3}q_0 y) \\ Q_{yy} &\simeq -\cos(2q_0 x) - \frac{1}{2} \cos(q_0 x) \cos(\sqrt{3}q_0 y) \\ Q_{yz} &\simeq -\sin(2q_0 x) - \sin(q_0 x) \cos(\sqrt{3}q_0 y). \end{aligned} \quad (11)$$

Finally, there are two possible hexagonal three-dimensional BPs identified in Ref. [13], which were found to be stable in the case of positive dielectric constant which we consider here. For the first one, abbreviated as H_{3D}^a , we used:

$$\begin{aligned} Q_{xx} &\simeq -\frac{3}{2} \cos(q_0 x) \cos(\sqrt{3}q_0 y) + \frac{1}{4} \cos(q_0 z) \\ Q_{xy} &\simeq -\frac{\sqrt{3}}{2} \sin(q_0 x) \sin(\sqrt{3}q_0 y) + \frac{1}{4} \sin(q_0 z) \\ Q_{xz} &\simeq \sqrt{3} \cos(q_0 x) \sin(\sqrt{3}q_0 y) \\ Q_{yy} &\simeq -\cos(2q_0 x) - \frac{1}{2} \cos(q_0 x) \cos(\sqrt{3}q_0 y) - \frac{1}{4} \cos(q_0 z) \\ Q_{yz} &\simeq -\sin(2q_0 x) - \sin(q_0 x) \cos(\sqrt{3}q_0 y). \end{aligned} \quad (12)$$

The starting condition for the second three-dimensional hexagonal phase, abbreviated as H_{3D}^b , is the same as the one used for H_{3D}^a , with the difference that all terms depending on either x or y (or both) have the opposite sign.

In order to calculate the phase diagrams in the three-dimensional parameter space spanned by τ, κ and e^2 , we follow the evolution of the free energy for the different configurations towards their (in general metastable) equilibria by solving Eq. 4. Once the \mathbf{Q} tensor reached a stationary state, we compare the free energy densities of the various structures and identify the lowest one as giving the true equilibrium. As already mentioned, this ignores the possibility of still lower values being achieved by phases that we have not considered, of which the most relevant are probably BPX (tetragonal) and BPIII (mentioned further below). In interpreting the phase diagrams shown below, the reader should bear in mind that their validity is thus restricted to the eighth phases (isotropic, nematic, cholesteric, BPI, BPII, H_{2D} , and the two H_{3D} phases) detailed above. We have restricted to these phases in line with the previous literature [2, 13]: introduction of other topologies may therefore lead to changes in this phase diagram.

An additional limitation to our work is as follows. We have already stated that the pitch parameter κ (via q_0) sets the preferred length scale for BP structures. However, the dimensionless number that relates the BP unit cell to q_0 is not known *a priori* but must be found as part of the free energy minimization. In numerical work, however, one can only simulate an integer number of unit cells within a periodic simulation domain. The procedure is then to fix the periodic domain but rescale the size of the physical volume that it represents by a so-called ‘redshift’ factor. One then finds the redshift that gives the lowest free energy as part of the dynamical minimization. For a completely general disclination lattice one requires an independent rescaling of each spatial dimension. For simplicity we here assume a single redshift factor to govern all three dimensions (*i.e.*, we assume a ‘cubic redshift’). This is in line with previous literature practice [2, 13, 23, 26], and it is the best we can currently do: an anisotropic redshift would effectively require a separate simulation for each aspect ratio chosen, and this would not be feasible with our current computational power. The assumption of a single redshift is exact for BPI and BPII only so long as these remain strictly cubic structures. In the presence of a field, both should acquire a tetragonal distortion which we cannot allow for; however, this effect is thought to be small [2]. The two H_{3D} structures are handled exactly only if the chosen aspect ratio of the unit cell box (which, for a cubic finite difference grid as used here, must be rational) coincides with the true one. Again, the error with our chosen value (26/15, see below) is expected to be minor.

It is useful to briefly sketch how the algorithm to determine the redshift works. The method we use was originally proposed in Ref. [15]. The free energy functional Eq. 3 comprises terms up to quadratic order in gradients

of the \mathbf{Q} -tensor: upon a rescaling of the unit cell dimension, $L \rightarrow L/r$, it is easy to see that the gradient term are rescaled by a factor of r per derivative. Therefore if we rescale $L \rightarrow L/r$, the new free energy becomes:

$$f(\mathbf{Q}) = r^2 A(\partial\mathbf{Q}^2) + rB(\partial\mathbf{Q}) + C. \quad (13)$$

The scaling factor r^* which minimizes the functional is then simply

$$r^* = -\frac{B}{2A}. \quad (14)$$

This observation provides a simple recipe to determine the redshift at every time step.

C. Numerical Aspects

Here we briefly present the computational details of our work. The size of the simulation boxes was $L_x = L_y = L_z = 32$ lattice sites for the cubic BPs BPI and BPII and for the cholesteric phase. To accommodate the hexagonal BPs we chose boxes of $L_x = 52, L_y = L_z = 30$ lattice sites for H_{2D} (although a cubic box would do in this case) and $L_x = L_z = 52, L_y = 30$ lattice sites for the two H_{3D} structures. These values were chosen as the closest approximation to the ratio $1 : \sqrt{3}$ which admits a ‘perfect’ hexagonal lattice such as the HCP structure of hard spheres. (As mentioned above, computational limitations did not allow us to explore different values of this aspect ratio parameter, which might be somewhat different for the true structure, even at $e = 0$.) The helical pitch was set to 16 lattice sites for the cubic BPs and for the cholesteric phase, and to 15 lattice sites for the hexagonal BPs. For BPI and BPII we generally simulated a box containing eight unit cells, to check for any (large scale) field-induced reconstruction; for the hexagonal BPs we used a single unit cell. As initial configurations we used a simple uniaxial helix for the cholesteric phase, together with the infinite chirality solutions Eqs. 9-12. The equation of motion of the order parameter Eq. 4 was solved by using a finite difference scheme [27] and a rotational diffusion constant $\Gamma = 0.3$ in simulation units. At each time step, the value of the redshift, equivalent of the optimal scaling factor r^* , was computed. This requires little extra calculation as the quantities A and B (see Eqs. 13-14) are needed for the free energy. Once we know the value of r^* , the unit cell needs to be ‘rescaled’. Instead of changing the actual simulation cell to be simulated, which would be inefficient and inaccurate, we rescale the elastic constants and q_0 by $1/r^*$ and r^* respectively. Typical runs to reach equilibration required 25,000 time steps. At the end of the run we compared the free energy densities in order to determine the equilibrium phase as the one with the lowest free energy density. To determine the onset of the nematic phase a visual check of the director field was performed.

III. RESULTS

A. Phase Diagrams

In this Section we present the phase diagrams obtained for cholesteric blue phases in the presence of an electric field. To validate our simulations, we first checked the field-free case, which was published in Ref. [15] using a code similar to ours (see also Ref. [14] for a version without the variable redshift).

The left panel curves in Fig. 1 were found to agree well with previous LB work [14, 15] except for minor deviations at the BPI-BPII boundary which could be explained by a slight difference in accuracy used. A few general remarks are in order to relate this phase diagrams to experimental ones, as well as to previous analytical predictions. At odds with the phase diagrams seen experimentally, such as the ones shown in [8], another BP, known as BPIII or the “Blue Fog” is missing. In experiments, the BPII region is entirely enclosed between BPI and BPIII, while in Fig. 1 it emerges as a region which is open towards higher chiralities. BPIII is believed to be an amorphous BP, which is stable at higher chiralities and is thermodynamically distinct from the others [8, 28, 29]. Although its structure is still a subject of discussion and has not been fully understood yet, there is some evidence that it might be closer to BPII than to the isotropic phase [8]. For theoretical attempts to understand the structure of BPIII see e.g. Refs. [30–32]. In principle our numerical approach *does* allow us to study large systems in regions in parameter space for which BPIII is expected, so that this limitation can be removed, at the cost of much more expensive simulations. (These must be many times larger than any shown here, so as to contain many cells of the aperiodic structure without strong finite size effects.) We accordingly defer our investigation of BPIII to a future publication [33].

It is interesting to compare our approach to an older realization of the Landau – de Gennes theory [2, 3, 12]. Within this approach the existence of field-stabilized hexagonal blue phases was first predicted. As mentioned in the introduction, the major drawback within this older framework was that, due to computational limitations at that time, the Q-tensor had to be expanded in a Fourier-series comprising several harmonics but only the $m = 2$ helicity mode. This simplification leads to the result that the last elastic term in Eq. (3) does not contribute to the phase diagram, which we believe is at the root of the quantitative discrepancy with our simulations. As a consequence the semi-analytical theory found the incorrect sequence of blue phases in the phase diagram. These earlier results are displayed in the right panel of Fig. 1. Remarkably, our approach shows instead the correct sequence (cholesteric / BPI / BPII) beneath the boundary to the isotropic state. Furthermore, in the earlier approximate approach BPII appears adjacent to the cholesteric phase and BPI occurs at considerably lower temperatures than in the full numerical phase diagram reported here

and in Refs. [14, 15]. Another important aspect is that the O_5 structure, which is predicted theoretically (see e.g. Ref. [12]) but not observed experimentally so far, is relegated to higher chiralities than the ones considered in our phase diagrams. For a long time these issues cast some doubt on the appropriateness of the Landau – de Gennes theory for describing blue phases, but it is now clear that this functional is actually in good qualitative agreement with experiments, and that the inconsistencies with observations were essentially a drawback of the approximations previously employed.

We turn now to the role of applied fields, $e \neq 0$, which forms the main focus of the current work. Figures 2-3 show phase diagrams in chirality-temperature plane for increasing field strengths $e = 0.2$ and $e = 0.3$. We can identify three main effects of the external field on the phase boundaries. First of all, in the region where the isotropic phase appeared in the field-free case, the system becomes oriented under the influence of the external field, forming a paranematic phase (N). This applies as well for the low-chirality part of the ordered region, where a nematic phase now appears in place of the cholesteric phase. For increasing field strengths the low-chirality nematic-cholesteric phase boundary and the cholesteric phase itself both move towards the right hand side of the phase diagram, *i.e.*, to higher chiralities. Secondly, increasing the value of the electric field leaves the BPI-BPII phase boundary almost unchanged, an interesting feature which has also been observed in experiments [24]. The extent of the cholesteric phase is more or less retained. The BPI region gets therefore overtaken by the cholesteric phase and its phase boundaries move towards lower temperatures. Finally, very close to the BP-nematic boundary a pocket of hexagonal blue phases opens up. The right panel in Fig. 2 display where Hornreich and Shtrikman [2] predicted these stable hexagonal BPs at the same field strength. Our results again suggest that their theoretical approach works well in terms of the general location of these phases, but quantitatively it suffers from the limitations of the approximations used. Our more accurate numerics show that while a transition from the H_{3D} phases to H_{2D} can arise under increasing field strength (see Fig. 4 below), the series of transitions most often observed is $H_{3D}^b \rightarrow H_{3D}^a \rightarrow H_{2D}$. We further predict that the boundary between H_{3D}^b and BPII, the closest among the cubic BPs, should be straight both in the (κ, τ) plane. Finally, we confirmed the observation from earlier work that H_{2D} is closer to the nematic phase with respect to the other hexagonal phases: this is perhaps expected as H_{2D} has a symmetry plane perpendicular to the field direction and its character is therefore closer to that of a nematic than that of the other BPs. As the stability region of the O_5 structure is outside the chirality range we considered at zero field, we have not pursued its study further at non-zero field (we expect an electric field to destabilise it, as happens with the other cubic phases).

Another way to visualize the phase behavior, especially to determine the experimentally relevant critical

field strength for the switching into the nematic state, is to perform cuts through the τ, κ, e parameter space for selected chiralities κ . Fig. 4 and 5 show phase diagrams in field-temperature plane for $\kappa = 1.0$ and $\kappa = 1.5$ respectively. A comparison with the semi-analytical calculations of Ref. [12] shows that their phase boundaries are roughly in the same place as ours, except that a BPI phase is entirely missing in the relevant parameter region. The near horizontal BPI- BPII boundary seen experimentally in [24] is very well reproduced in our findings.

B. Visualization of the BPs

One of the most common ways to characterize the structure of liquid crystals is to visualize their local order, *e.g.*, via their director field. Within the Q-tensor theory a director can be defined according to Eq. 2 as the normalized length vector which belongs to the largest eigenvalue of the Q-tensor. However, as the preferred configuration in BPs is an arrangement of double twist cylinders involving a highly complex network of disclinations, it is almost impossible to visualize their structure in more than two dimensions in this way. Perhaps the clearest alternative is then to show the defect structure itself, which has become the usual way to portray BP structures. In our simulations, this can easily be achieved by setting a threshold for the scalar order parameter q (defined as the maximum eigenvalue of the tensor order parameter) and imaging the resultant isosurface, which divides ‘defect’ (low q) from ‘non-defect’ (high q) zones. Although rather simple, this method works remarkably well and we use it here due to its simplicity of implementation. The following figures 6-9 show therefore isosurfaces of the scalar order parameter q .

Fig. 6 represents a unit cell of the hexagonal two-dimensional BP H_{2D} in the field-free case $e = 0$ at $\tau = 0.75, \kappa = 1.5$. The isosurface correspond to a value $q = 0.11$. This is a metastable configuration, because the H_{2D} phase is only found to be the equilibrium phase for fields $e \approx 0.3$. Clearly recognizable is the hexagonal arrangement of the disclination lines. These are oriented along the z -direction, which is the direction of the applied external field. (With a field on, neither of the hexagonal BPs could be maintained with disclinations perpendicular to the field.) Note that a unit cell of the hexagonal structures carries a full turn of the director when one passes through it along the x - or y -direction, in contrast with a half turn in the cases of the cubic blue phases (this can be seen, *e.g.*, from checking the periodicity of the tensorial order parameter in Eqs. 9-12).

If the external field is switched on, as shown in Fig. 7, the regions with low order become slightly larger and the disclination tubes facet. The magnitude of the order parameter at its maxima is found to be larger than in the field-free case.

The situation is more complicated for the hexagonal three-dimensional BPs, H_{3D}^a and H_{3D}^b . Fig. 8 shows a

metastable example of H_{3D}^a at $\tau = 0.6, \kappa = 1.5$ and $e = 0$; one can readily recognize a hexagonal arrangement if viewing along the z direction, *i.e.* perpendicular to the xy plane. However, when viewed from other directions the structure looks quite intricate. The general appearance, but not the topology, of the structure slightly depends on the value of the threshold of the scalar order parameter q ; we have chosen a threshold of $q = 0.15$.

Fig. 9 shows the same phase with external field. The defect regions along the field direction merge and increase in their extent. Similarly, in the xy symmetry plane the domains with higher order around the center of the voids increase in size.

Fig. 10 and 11 instead show the other 3D hexagonal phase, H_{3D}^b , both without and with a field. Again the former configuration is metastable, while the latter is stable. With respect to H_{3D}^b , the disclination lines making up the H_{3D}^b network do not merge at any point (at least for the values of the threshold, chosen, again $q = 0.15$). These lines are twisted and arranged onto parallel planes, the orientation of neighboring planes being about 60° consistently with the overall hexagonal symmetry. When a field is applied and the H_{3D}^b phase is stable, the disclinations twist up (this is more evident when viewed in a direction perpendicular to the xy plane – compare the top panels of Fig. 10 and 11).

The result that the BPI-BPII phase boundary in Fig. 4 and 5 remains almost constant with increasing field strength (before the system enters first the cholesteric and then the nematic phase) has its counterpart in the near constancy of the disclination network of these structures as the field is varied. Indeed the cubic BPs appear to be much more stable than the hexagonal BPs and are hardly deformed by the influence of the external field. The top picture in Fig. 12 gives the isosurface $q = 0.22$ of the order parameter in BPI, whereas the picture at the bottom shows the isosurface $q = 0.15$ in BPII. The cyan surfaces depict the field-free case, while the magenta parts show results for the field strength $e = 0.3$. It is clear that the disclination network changes only slightly, and the isosurfaces are only slightly displaced in direction of the external field. (Recall however that our single-redshift approach excludes any anisotropic distortion of these structures that could arise at high field strengths.)

IV. CONCLUSIONS

We have presented extensive numerical simulations to investigate the phase diagram of cholesteric blue phases in an electric field. We have considered the case of a positive dielectric anisotropy, and we have for computational simplicity taken into account only isotropic deformations of the unit cell for each structure. While this leaves out by necessity phenomena like the “anomalous electrostriction” of BPI [6, 16, 17], this is a good starting point, particularly for comparisons with the earlier literature which often employed this approximation.

We confirm in their main qualitative aspects the predictions of Refs. [2, 3], which were found by a semi-analytical approximation which led to the phase diagram being independent of one of the elastic constants. These works predicted that intermediate values of the electric field stabilizes two new hexagonal blue phases, one with 2-dimensional and another one with 3-dimensional symmetry. With respect to previous literature, we were able to refine the phase diagrams in two important ways. First, we find that the blue phase regions extends to significantly lower values of chirality than previously estimated. Second, we have established which of the cubic blue phases, BPI or BPII, is stable for a fixed value of electric field, chirality and temperature. At a given chirality value, we found that the boundary between BPI and BPII does not appreciably depend on temperature, in agreement with experimental results. Finally we have seen that the disclination lattices of the hexagonal blue phases modify quite strongly as the field is increased, in contrast to what happens for the cubic blue phases which, up until close to the transition to the nematic or cholesteric state, are not greatly affected in structure by applied fields.

To improve further the accuracy of our phase diagrams, while remaining within the general framework of the Lan-

dau – de Gennes approach, it would be necessary not only to relax the ‘cubic redshift’ assumption, but also to go beyond the one elastic constant approximation. This would allow further insight into the adequacy of the Landau – de Gennes theory in quantitatively accounting for the experimental phase behavior. Meanwhile, our work lays a useful foundation for future computer simulations of blue phases in electric fields, addressing for instance the switching dynamics of blue phase devices. To study dynamics, rather than the equilibrium phase behavior addressed here, one must however use the full momentum-conserving equations of motion. To this end, our finite difference code has already been married to a lattice Boltzmann approach [20, 21] creating a hybrid code with which we plan to address such issues in the near future.

Acknowledgments

We acknowledge support by EPSRC grants EP/E045316 and EP/E030173, and useful discussions with G. P. Alexander and E. Orlandini. M.E.C. holds a Royal Society Research Professorship.

-
- [1] D. C. Wright and N. D. Mermin, *Rev. Mod. Phys.* **61**, 385 (1989).
 - [2] R. Hornreich, M. Kugler, and S. Shtrikman, *Phys. Rev. Lett.* **54**, 2099 (1985).
 - [3] R. Hornreich and S. Shtrikman, *Mol. Cryst. Liq. Cryst.* **165**, 183 (1987).
 - [4] P. Pieranski, P. E. Cladis, and R. Barbetmassin, *Journal de Physique Lettres* **46**, L973 (1985).
 - [5] P. Pieranski and P. E. Cladis, *Phys. Rev. A* **35**, 355 (1987).
 - [6] G. P. Alexander and D. Marenduzzo, *Europhys. Lett.* **81**, 66004 (2008).
 - [7] H. S. Kitzerow, *Mol. Cryst. Liq. Cryst.* **202**, 51 (1991).
 - [8] P. Crooker, *Liquid Crystals* **5**, 751 (1989).
 - [9] H. J. Coles and M. N. Pivnenko, *Nature* **436**, 997 (2005).
 - [10] H. Kikuchi, M. Yokota, Y. Hisakado, H. Yang, and T. Kajiyama, *Nat. Mater.* **1**, 64 (2002).
 - [11] H. Kikuchi, S. Hirata, and K. Uchida, *Mol. Cryst. Liq. Cryst.* **465**, 283 (2007).
 - [12] H. Grebel, R. Hornreich, and S. Shtrikman, *Phys. Rev. A* **30**, 3264 (1984).
 - [13] R. Hornreich and S. Shtrikman, *Phys. Rev. A* **41**, 1978 (1990).
 - [14] A. Dupuis, D. Marenduzzo, and J. M. Yeomans, *Phys. Rev. E* **71**, 011703 (2005).
 - [15] G. P. Alexander and J. M. Yeomans, *Phys. Rev. E* **74**, 061706 (2006).
 - [16] H. Stark and H. R. Trebin, *Phys. Rev. A* **44**, 2752 (1991).
 - [17] M. Zelazna, L. Longa, H. R. Trebin, and H. Stark, *Phys. Rev. E* **57**, 6711 (1998).
 - [18] P. G. de Gennes and J. Prost, *The Physics of Liquid Crystals (2nd Edition)* (Clarendon Press, Oxford, 1993).
 - [19] A. Dupuis, D. Marenduzzo, E. Orlandini, and J. M. Yeomans, *Phys. Rev. Lett.* **95**, 097801 (2005).
 - [20] O. Henrich, D. Marenduzzo, K. Stratford, and M. E. Cates, doi:10.1016/j.camwa.2009.08.047 (2010).
 - [21] M. E. Cates, O. Henrich, D. Marenduzzo, and K. Stratford, *Soft Matter* **5**, 3791 (2009).
 - [22] A. Tiribocchi, N. Stella, A. Lamura, and G. Gonnella, *Phys. Rev. E* **80**, 026701 (2009).
 - [23] D. Lubin and R. M. Hornreich, *Phys. Rev. A* **36**, 849 (1987).
 - [24] H. Stegemeyer and F. Porsch, *Phys. Rev. A* **30**, 3369 (1984).
 - [25] R. Memmer, *Liquid Crystals* **27**, 533 (2000).
 - [26] R. Hornreich and S. Shtrikman, *Mol. Cryst. Liq. Cryst.* **165**, 183 (1987).
 - [27] D. Marenduzzo, E. Orlandini, M. Cates, and J. Yeomans, *Phys. Rev. E* **76**, 031921 (2007).
 - [28] Z. Kutnjak, C. W. Garland, J. L. Passmore, and P. J. Collings, *Phys. Rev. Lett.* **74**, 4859 (1995).
 - [29] E. P. Koistinen and P. H. Keyes, *Phys. Rev. Lett.* **74**, 4460 (1995).
 - [30] R. M. Hornreich and S. Shtrikman, *Phys. Rev. Lett.* **56**, 1723 (1986).
 - [31] D. Rokhsar and J. Sethna, *Phys. Rev. Lett.* **56**, 1727 (1986).
 - [32] J. Englert, L. Longa, H. Stark, and H.-R. Trebin, *Phys. Rev. Lett.* **81**, 1457 (1998).
 - [33] O. Henrich, D. Marenduzzo, K. Stratford, and M. Cates (in preparation).

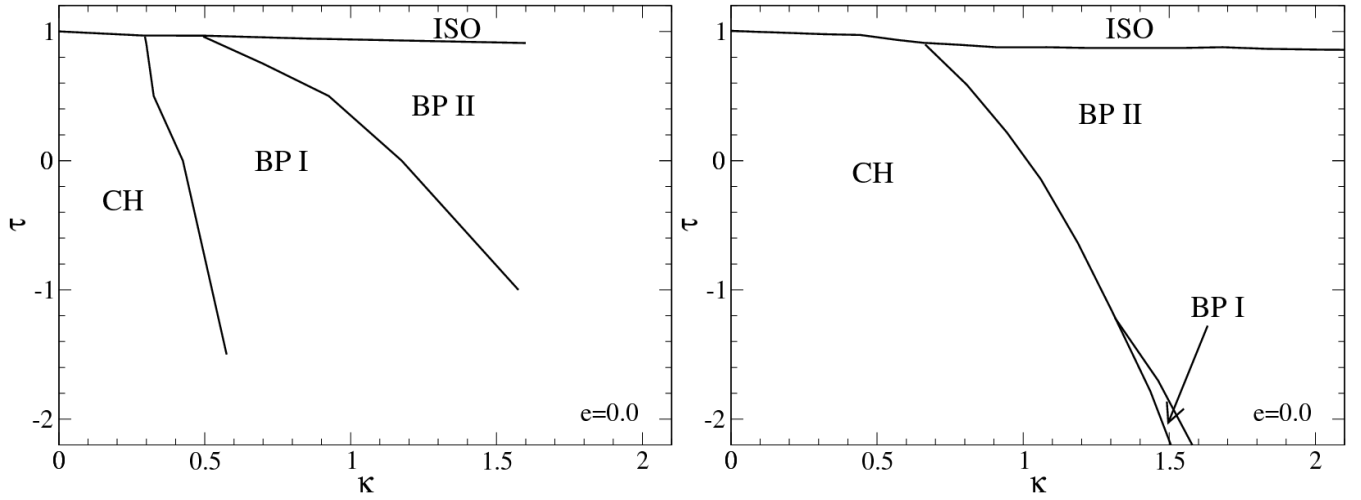


FIG. 1: Phase diagrams in chirality-temperature plain for $e = 0$, as found within our approach (left) and in Ref. [2] (right). Typically, redshift values for BPI were smaller than for BPII, e.g. at $\tau = 0$, for $\kappa = 0.55$ and $\kappa = 1.1$ BPI was found to be stable, with a redshift r equal to, respectively, $r = 0.7$ and $r = 0.76$; while for $\kappa = 1.4$ BPII was stable and $r = 0.88$.

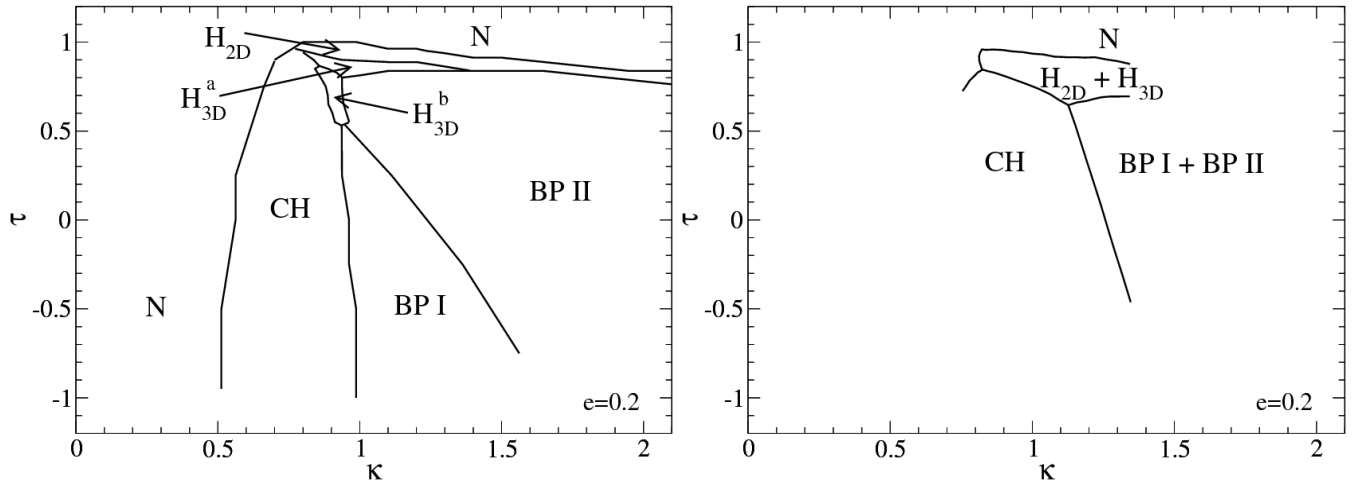


FIG. 2: Phase diagrams in chirality-temperature plain for $e = 0.2$, as found with our approach (left) and in Ref. [2] (right). Redshift values were typically smaller for BPI than for BPII, and smaller for cubic blue phases than for hexagonal ones: e.g. for BPI at $\tau = 0$, and $\kappa = 1.1$, $r = 0.82$; for BPII at $\tau = 0$ and $\kappa = 1.4$, $r = 0.89$; for H_{2D} at $\tau = 0.95$ and $\kappa = 0.9$, $r = 0.96$; for H_{3D}^a at $\tau = 0.9$ and $\kappa = 0.9$, $r = 0.935$; for H_{3D}^b at $\tau = 0.8$ and $\kappa = 0.9$, $r = 0.91$. Note that for smaller values of e we reproduce electrostriction and the redshift decreases albeit very slightly, in agreement with previous theoretical and numerical literature [6, 23].

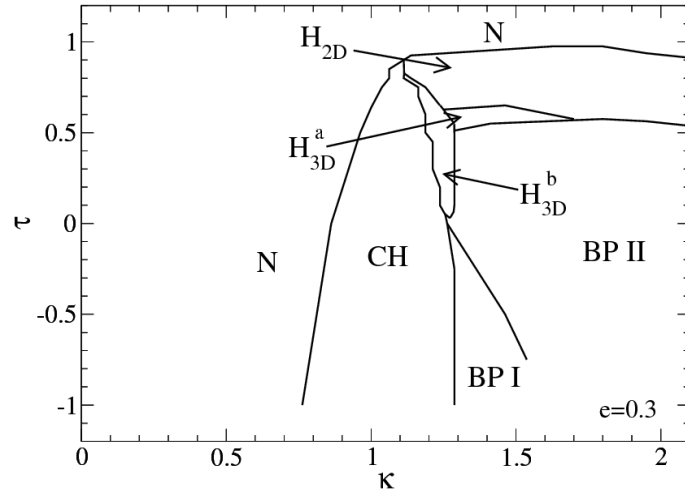


FIG. 3: Phase diagram in chirality-temperature plain for $e = 0.3$.

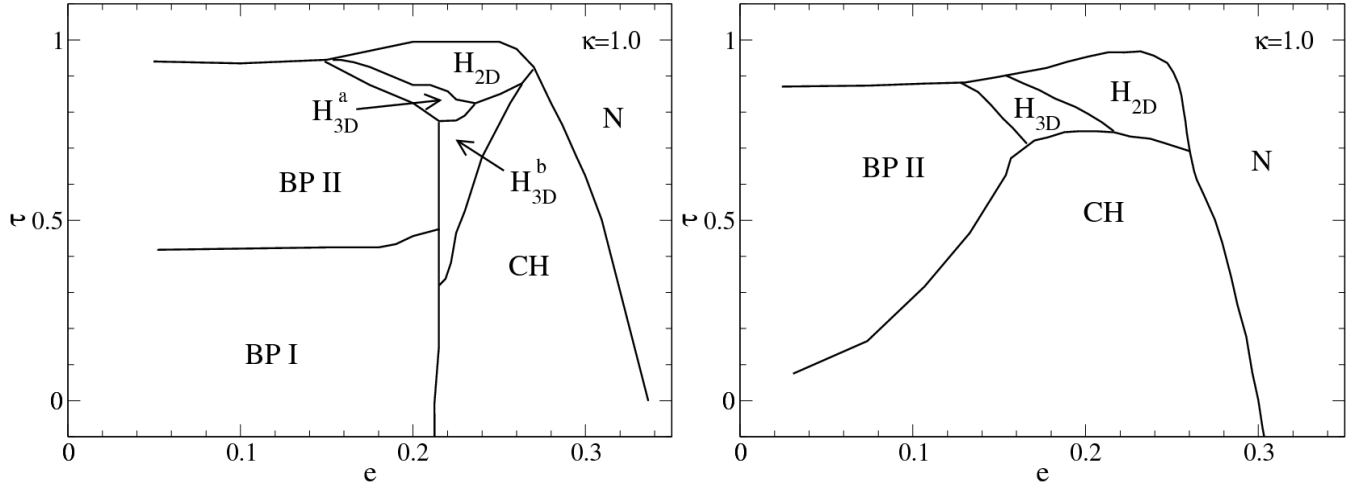


FIG. 4: Phase diagrams in field strength-temperature plain for $\kappa = 1.0$ as found with our approach (left) and in Ref. [2] (right). Note that change in scale for τ .

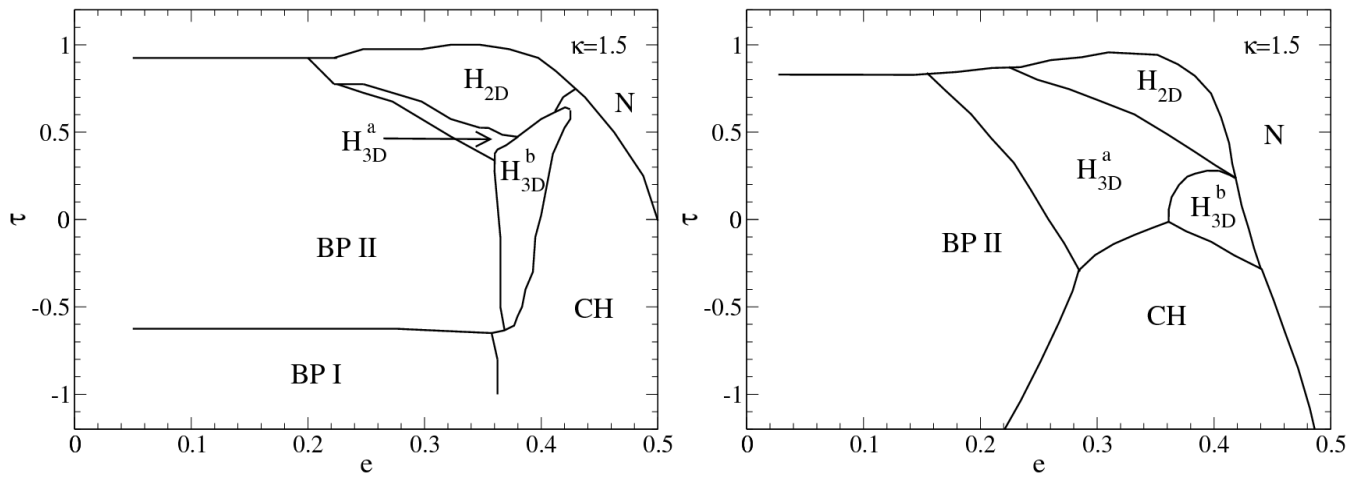


FIG. 5: Phase diagrams in field strength-temperature plain for $\kappa = 1.5$ as found with our approach (left) and in Ref. [2] (right).

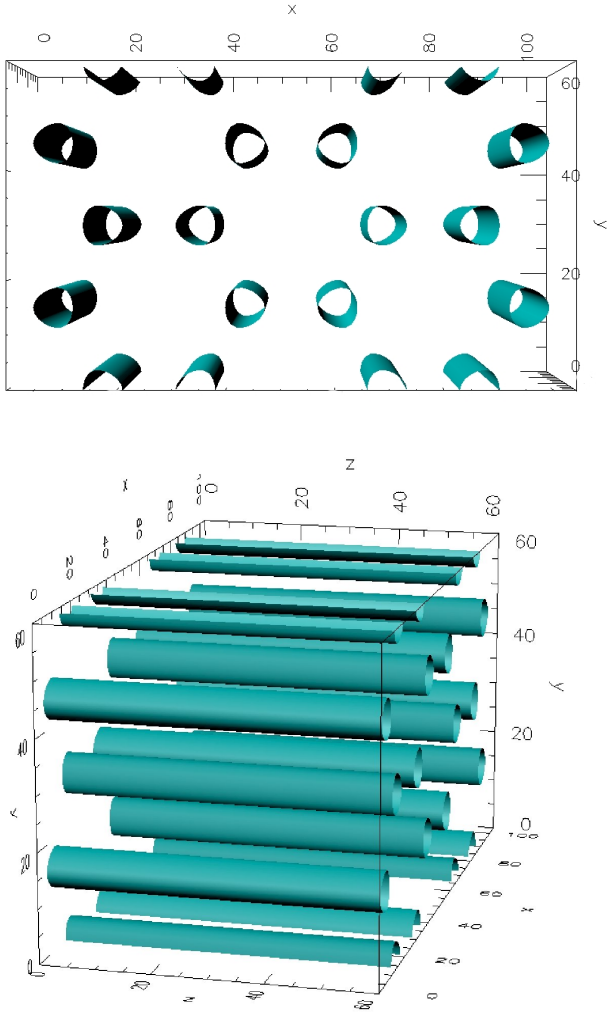


FIG. 6: Hexagonal-2D BP in equilibrium state at $\tau = 0.75, \kappa = 1.5, e = 0$. Each tube contains a disclination line.

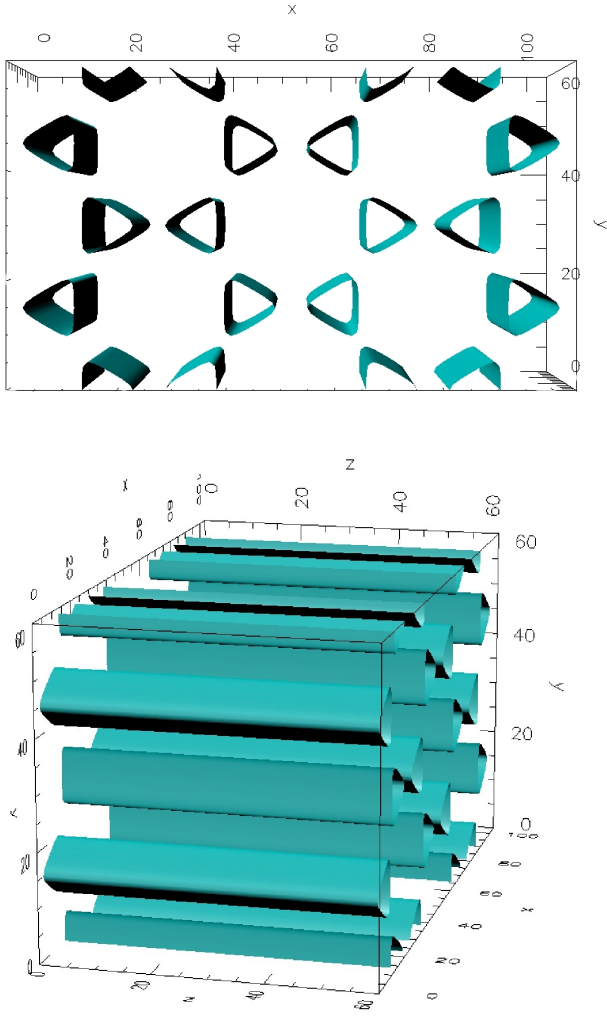


FIG. 7: Hexagonal-2D BP in equilibrium state at $\tau = 0.75, \kappa = 1.5, e = 0.3$.

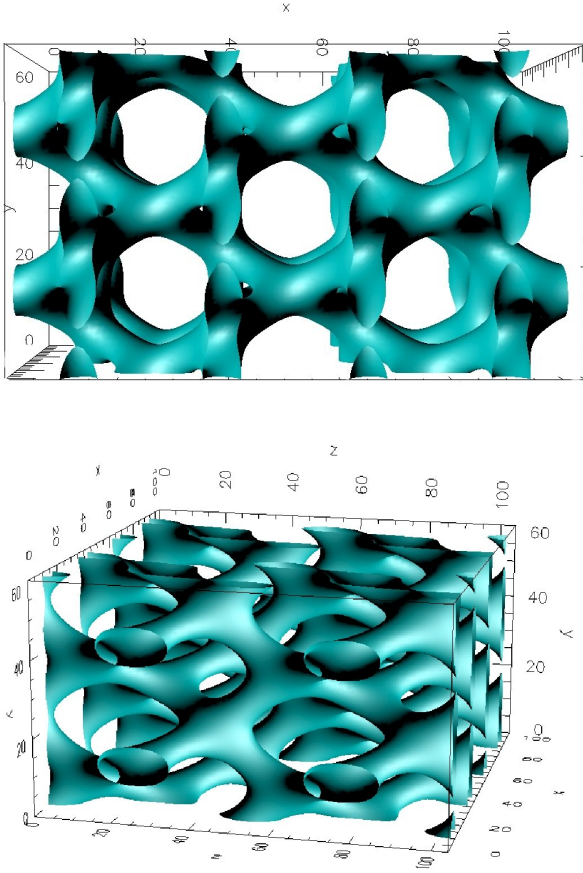


FIG. 8: Hexagonal-3Da BP in metastable state at $\tau = 0.6$, $\kappa = 1.5$, $e = 0$.

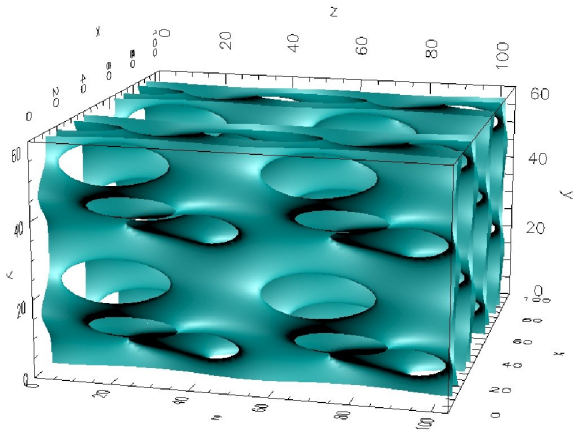
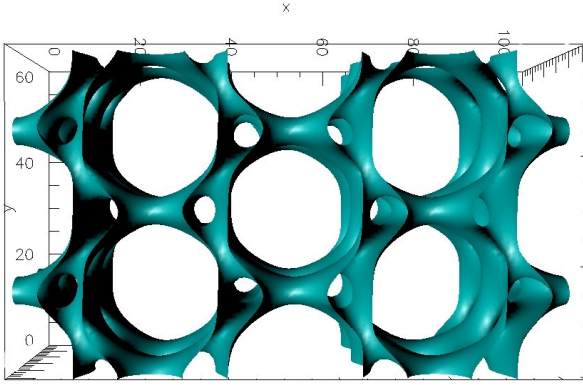


FIG. 9: Hexagonal-3Da BP in equilibrium state at $\tau = 0.5$, $\kappa = 1.25$, $e = 0.3$.

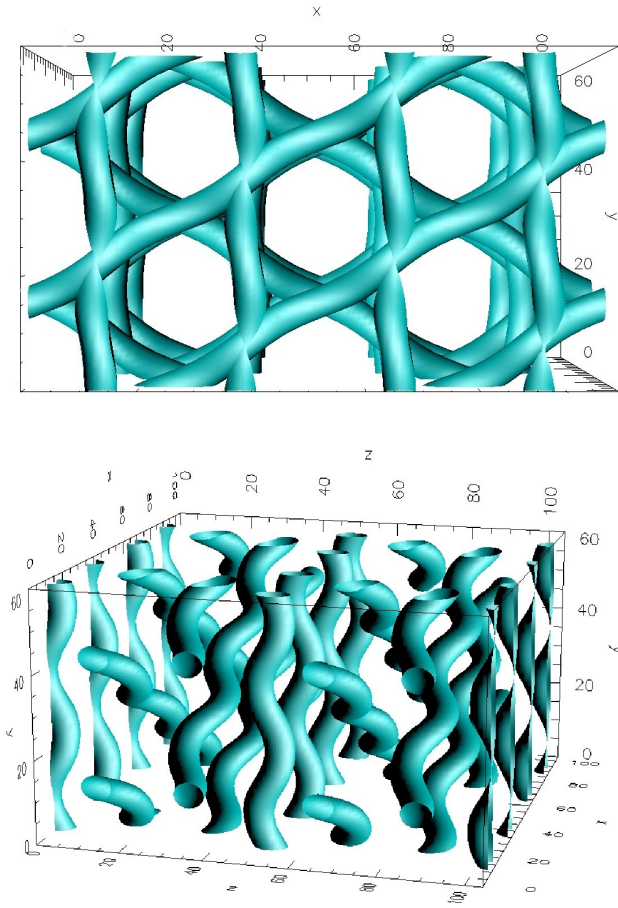


FIG. 10: Hexagonal-3Db BP in metastable state at $\tau = 0.5$, $\kappa = 1.25$, $e = 0$.

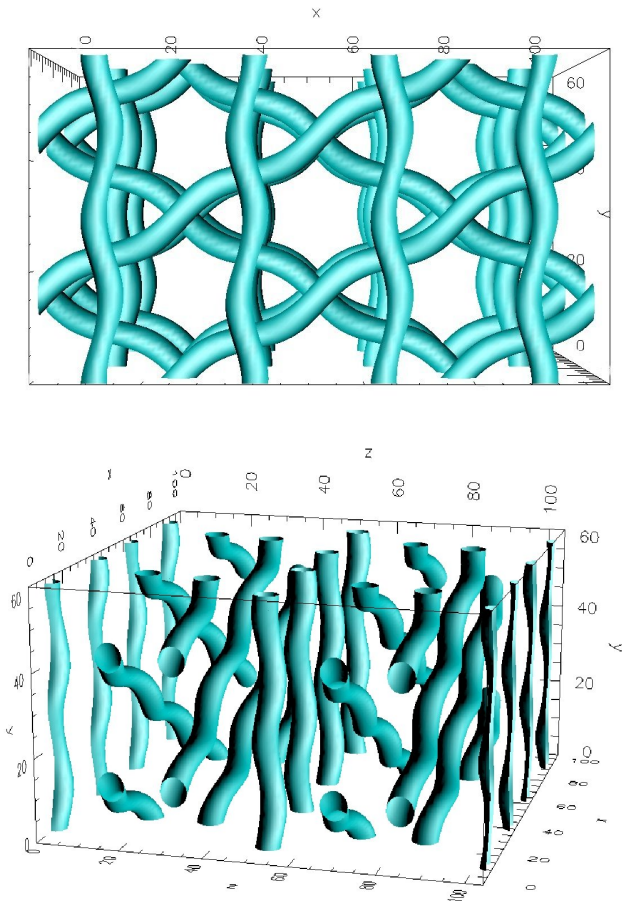


FIG. 11: Hexagonal-3Db BP in equilibrium state at $\tau = 0.6$, $\kappa = 1.5$, $e = 0.3$.

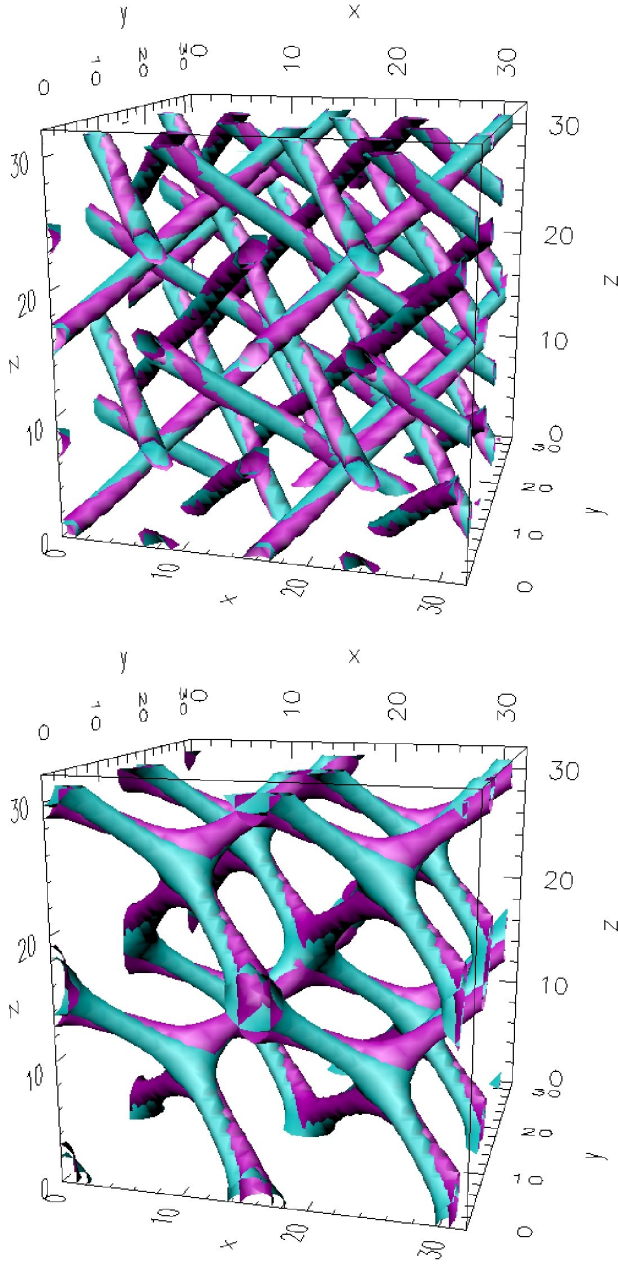


FIG. 12: BPI (top, at $\tau = -0.8, \kappa = 1.5$) and BPII (bottom, at $\tau = 0, \kappa = 1.5$) at $e = 0$ (cyan) and $e = 0.3$ (magenta).